Core hole processes in x-ray absorption and photoemission by resonant Auger-electron spectroscopy and first-principles theory

J. C. Woicik,[1] C. Weiland,[1] A. K. Rumaiz [iD],[2] M. T. Brumbach,[3] J. M. Ablett,[4] E. L. Shirley [iD],[5] J. J. Kas,[6] and J. J. Rehr [iD][6]

[1]*Material Measurement Science Division, Material Measurement Laboratory, National Institute of Standards and Technology, Gaithersburg, Maryland 20899, USA*

[2]*National Synchrotron Light Source II, Brookhaven National Laboratory, Upton, New York 11973, USA*

[3]*Materials Characterization Department, Sandia National Laboratories, Albuquerque, New Mexico 87185, USA*

[4]*Synchrotron SOLEIL, L'Orme des Merisiers, Saint-Aubin, 91192 Gif-sur-Yvette Cedex, France*

[5]*Sensor Science Division, Physical Measurement Laboratory, National Institute of Standards and Technology, Gaithersburg, Maryland 20899, USA*

[6]*Department of Physics, University of Washington, Seattle, Washington 98195, USA*

Electron–core hole interactions are critical for proper interpretation of core-level spectroscopies commonly used as analytical tools in materials science. Here we utilize resonant Auger-electron spectroscopy to uniquely identify exciton, shake, and charge-transfer processes that result from the sudden creation of the core hole in both x-ray-absorption and photoemission spectra. These effects are captured for the transition-metal compounds $SrTiO_3$ and MoS_2 by fully *ab initio*, combined real-time cumulant, and Bethe-Salpeter equation approaches to account for core hole dynamics and screening. Atomic charges and excited-state electron-density fluctuations reflect materials' solid-state electronic structure, loss of translational symmetry around the core hole, and breakdown of the sudden approximation. They also demonstrate competition between long- and short-range screening in a solid.

I. INTRODUCTION

Absorption of a photon and emission of an electron is not simply a two-particle process, as demonstrated by the rich satellite and multiplet structures observed in x-ray absorption spectroscopy (XAS) and x-ray photoelectron spectroscopy (XPS) spectra. Multiplets arise from the angular momentum coupling of the core hole with the unpaired valence electrons or magnetic structure of the atom, while satellites arise from the discrete valence excitations that occur in response to its sudden creation [1]. For noble gases, satellites involve transitions between electronic states within the ionized atom ("shake-up"), or multiple ionizations that promote additional electrons into the continuum ("shake-off") [2,3]. Because of the chemical bonding in molecules and solids, it has been suggested that electrons can even *hop* between atoms during core photoionization, giving rise to what have become known as "charge-transfer" shake-up excitations [4–6].

Historically, the theory of x-ray satellite structure has been based primarily on the sudden approximation [2,3,7–9]. That is, it is assumed that the N particle Hamiltonian changes from $H(N)$ to $H'(N-1)$ because of the sudden creation of the core hole, while the many-electron wave function otherwise varies continuously [10]. The initial state of the photoionized atom is therefore taken to be the ground state of the neutral system less the photoelectron. This state can be expanded in eigenstates of the ionized system H' in terms of overlap integrals:

$$\Psi(N-1) = \sum_{n=0}^{\infty} \langle \Psi'_n(N-1)|\Psi(N-1)\rangle \Psi'_n(N-1). \quad (1)$$

The overlapping part of $\Psi(N-1)$ with $\Psi'_0(N-1)$ contributes to the main photoemission line, whereas the contributions for $n > 0$ are satellites. Photoemission can therefore directly probe many-body interactions and electron correlation in atoms, molecules, and solids.

While satellites in atomic and small molecular systems have been interpreted within the sudden and Hartree-Fock approximations [8], satellites in solid-state systems and especially the transition-metal compounds have remained contentious. Early work attributed the primary or "main" cation photopeak to direct photoionization and its satellite to monopole ligand-to-metal charge transfer [4–6]. Later theoretical studies, however, assigned the primary peak to a "well-screened" core hole, screened by the transfer of an electron from a ligand atom to the metal atom, and its satellite to an "unscreened" core hole or direct photoionization [11–14]. These theories, however, often consider small clusters and solve a model Hamiltonian within an Anderson-impurity limit that incorporates *ad hoc* fitting parameters in addition to arbitrary long-range screening channels, each of which carries its own free parameters [15].

Recently, a *first-principles* theory utilizing the cumulant representation of the core hole Green's function in a

real-time, time-dependent density-functional-theory (RT-TDDFT) calculation has been developed for charge-transfer satellites in solid-state systems [16]. To date, this approach has predicted the Ti 2*p* satellite structure of TiO$_2$ [16]; the Ni 1*s*, 2*p*, and 3*s* satellite structures of NiO [16]; and the doping dependence of the metallic screening for binary metallic alloys [17]. It has also successfully been applied to the plasmon structure of Si [18] and Na [19] where the *GW* approximation for the self-energy is known to fail. The method has advantages over more traditional frequency-based formalisms because it is a *real-time*, *real-space* approach that follows the time evolution of the many-body system in addition to that of the excited-state electron densities, as was demonstrated for the high energy satellite structure of TiO$_2$ [16]. Considering this relatively new development, a robust experimental method that can uniquely distinguish the physical nature of these many-body excitations is required to aid further development of such first-principles methods that model both ground and excited-state electronic structures.

In this paper, we apply the resonant Auger effect to the excited-state electronic structure of transition-metal compounds. We demonstrate that the technique can uniquely identify exciton, shake, and charge-transfer processes that result from the sudden creation of the core hole in both XAS and XPS spectra. Ironically, it is the breakdown of the sudden approximation [Eq. (1)] on energetic grounds [8] that affords this unique experimental measurement: As stated by Hedin, "At photon energies which are barely large enough to take the electron above the Fermi level there is clearly no energy available to make satellites (or line-shape asymmetry)" [20]. Also note Siegbahn's discovery that the Auger deexcitation spectrum of a core hole retains information of the initial charge state of the photoionized atom [21]. Therefore, by directly measuring the electrostatic contribution to the excited-state Auger decay as a function of photon energy above a core-ionization threshold, the direction and nature of the charge transfer associated with the eigenstates of Eq. (1) can be uniquely determined. This simple physical interpretation is gleaned from argon gas where the Ar 3*p* → 4*p* shake-up transition is observed as a "satellite" peak in the Auger spectrum occurring at 15-eV-higher binding energy than the main or "diagram" Auger line [22]. This satellite "turns on" in the Auger spectrum at the "shake" threshold which is 25 eV above the main 1*s* → 4*p* transition [23,24].

Our paper is structured as follows. First, we describe the real-time cumulant and Bethe-Salpeter equation (BSE) calculations and give experimental details. Second, we present the Ti 1*s* and the S 1*s* XPS spectra for SrTiO$_3$ and MoS$_2$. These materials are ideal for a comparative Auger study of x-ray satellites because they enable investigations of the excitation and deexcitation spectra of the 1*s* core hole for the anion and the cation of transition-metal complexes under similar experimental conditions; i.e., with a Si(111) double-crystal monochromator as the x-ray excitation source and examining core-core-core K-$L_{2,3}L_{2,3}$ Auger-electron decay. We find that the RT-TDDFT calculation of the cumulant accurately predicts the energies, intensities, and overall satellite structures observed in the XPS.

Third, we compare the 1*s* (K-edge) XAS for both materials with BSE calculations [25] with and without inclusion of the electron–core hole interaction. The utility of this procedure has been demonstrated previously for SrTiO$_3$ [26] and MoS$_2$ [27], but the former employed large ionic supercells rather than the BSE, so it is of further importance to test the predictive power of more modern methods. It has been stated that a redistribution of oscillator strength should always be observed in XAS because of the core hole, but it is only in the case of a bound exciton that energy shifts are observed [28]. Our analysis therefore reveals the Coulomb interaction between the 1*s* core hole and the excited photoelectron in the conduction band. Furthermore, while the BSE goes beyond the single-particle approximation, it does not include many-electron excitations. We incorporate these effects into the BSE by convolution with the cumulant calculation of the self-energy for the core hole Green's function [29–31]. As stated by Stern *et al.* [32], the dipole sum rule dictates that the total absorption must remain the same in the presence of satellites; therefore, these multielectron effects account for the loss of absorption in the primary channel. The cumulant is found to knock down the overstated intensity of the signature edge with redistribution of oscillator strength to the satellite binding energies, thereby greatly improving the predictive power of the BSE.

Fourth, we present our Ti and S K-$L_{2,3}L_{2,3}$ resonant Auger spectra. Remarkably, we find that the satellite cross section so measured for MoS$_2$ exhibits the same XAS oscillations as the signature edge, but it is shifted upwards in energy by the satellite binding energy. This observation confirms Stern *et al.*'s ansatz [32], and it gives direct experimental justification for the convolution procedure utilized. In addition, we find that the energy shift of the Auger peak at resonance approximates the BSE prediction of the Coulomb interaction between the core hole and the excited photoelectron in the conduction band [33], and it is this relationship that allows us to experimentally determine the nature of satellite charge transfer. Counter to previous theoretical assignments of well-screened and unscreened photopeaks, our data demonstrate that the assignment should be closer to "screened" and "over-screened" photopeaks. While this result may seem surprising, it is consistent with the idea that the core hole should always be screened in the ground state of the $N-1$ electron system, at least in a solid, while the satellite (for a metal photoemitter) can be either underscreened (metal-to-ligand charge transfer) or overscreened (ligand-to-metal charge transfer). In addition, the shifts of the Auger peaks for photon energies equaling the satellite binding energies coincide with the observed shifts at resonance, and this result is consistent with a simple electrostatic model of core hole screening.

Fifth, we present the theoretical atomic charges and their excited-state density fluctuations around the photon-absorbing atom and its near neighbors and interpret them within the context of the materials' solid-state electronic structure. The fluctuations reveal the broken translational symmetry around the core hole and the breakdown of the sudden approximation [Eq. (1)]. They also demonstrate the competition between long- and short-range screening that occurs in a solid.

Lastly, we conclude with a brief synopsis.

II. REAL-TIME CUMULANT AND BETHE-SALPETER EQUATION CALCULATIONS

Theoretically, the XPS is related to the core hole Green's function [20], which we calculate via the real-time cumulant approach [16]. Within the cumulant approximation, the core hole Green's function is represented as an exponential in time $G_c(t) = -i \exp[i\varepsilon_c t + C(t)]$, where ε_c is the core-level binding energy associated with the main peak in XPS and $C(t)$ is the cumulant, which contains the information about the many-body excitations (satellites). The cumulant is calculated in terms of the real-space density response to the sudden appearance of the core hole, which allows for real-space analysis of the excitations involved. The quantity of interest for XPS is the spectral function $A_c(\omega) = -(1/\pi) \operatorname{Im} G_c(\omega)$.

While the core hole-spectral function treats the excitations produced via coupling to the core hole (intrinsic excitations) and can describe XPS, a correct picture should include several other effects. First, the amplitude of satellites is expected to be modified by excitations that arise from coupling of the core hole to the photoelectron as it travels through the material (extrinsic excitations), as well as by interference between the two types of excitation. We have found that these effects can be modeled via a single, energy independent amplitude factor multiplying the satellite strength. However, since extrinsic and interference effects tend to cancel, here we choose to disregard such effects in order to maintain model independence. Second, a background function describing other inelastic processes, such as Auger and vibrational effects, was added according to the Shirley method [34]. Third, lifetime-broadening effects were included for valence excitations (satellite features) and the core hole via Lorentzian-broadening parameters (half widths) Γ_v and Γ_c, respectively, and an additional overall broadening Γ_{exp} was included to match the experimental resolution of the main peak.

In order to limit spurious interactions between core holes, the RT-TDDFT calculation of the cumulant was performed on a $3 \times 4 \times 4$, 240 atom supercell for $SrTiO_3$ and a $4 \times 2 \times 1$, 96 atom orthogonal supercell for MoS_2. The lifetime broadening of the satellites Γ_v was set to 0.5 eV for all calculations, and the broadening of the main peak $\Gamma_c + \Gamma_{exp}$ was set to 0.75 eV for $SrTiO_3$ and 0.38 eV for MoS_2.

Ti K-edge XAS for $SrTiO_3$ and S K-edge XAS for MoS_2 were calculated using the known crystal structures for $SrTiO_3$ [35,36] and MoS_2 [37], the latter of which includes vibrational motion at room temperature. The x-ray near-edge extinction coefficient, $\mu(\varepsilon) = -\operatorname{Im}\langle 0|O^\dagger[\varepsilon + i\gamma(\varepsilon) - H]^{-1}O|0\rangle$, involves the ground state $|0\rangle$, light-matter interaction O, and core-excited Hamiltonian H. H includes electron dynamics through the band structure, the core-level binding energy, and electron–core hole interaction. We calculated $\mu(\varepsilon)$ using a BSE method as implemented in the OCEAN code [38]. The broadening $\gamma(\varepsilon)$ simulated experimental resolution [39], electron-damping effects [40], and core hole-lifetime damping [41]. Further details of the calculations were provided in Ref. [35] for $SrTiO_3$ and in Ref. [27] for MoS_2. We also amplified the BSE calculations by application of the cumulant-based spectral function according to Ref. [42] as described

below. In doing so, the cumulant correction supplants the self-energy damping of the electron.

III. EXPERIMENTAL DETAILS

The experiments were performed at the NIST beamlines X24A and SST-2 of the National Synchrotron Light Source I and II, Brookhaven National Laboratory. XPS data were collected using the Si(111) reflection from a double-crystal monochromator and a hemispherical electron analyzer that had its acceptance cone oriented parallel to the x-ray electric-polarization vector of the incident beam. The Si(220) reflection was used for the Ti K-edge XAS measurements, and the Si(111) reflection was used for the S K-edge XAS measurements. XAS data were recorded by total-electron yield, except where indicated otherwise. Details of the beamlines, vacuum systems, and experimental procedures have been presented previously [27,43–45].

IV. RESULTS AND DISCUSSION

Figure 1(a) shows the Ti 1s XPS spectrum for $SrTiO_3$ recorded with photon energy $h\nu = 5600$ eV, and Fig. 1(b) shows the S 1s XPS spectrum for MoS_2 recorded with photon energy $h\nu = 3100$ eV. Both energies are approximately 630 eV above their respective materials' K edge. The insets of each figure show an expanded view of the satellite loss structures. The Ti 1s XPS displays the well-studied, high-energy satellite near 14 eV [46,47] and the more recently resolved, low energy satellite near 6 eV [45]. The S 1s XPS data show a complex, low energy manifold extending from 4 to 6 eV, and a more pronounced feature near 9 eV, which also has additional structure.

Both Figs. 1(a) and 1(b) compare the experimental satellite structures to the theoretical-loss curves obtained from the RT-TDDFT cumulant calculations [16]. The theoretical spectra have been aligned in binding energy and broadened theoretically to simulate experimental-Gaussian [39] and natural-Lorentzian [41] linewidths. The agreement between the experimental data and the first-principles simulations, both in general structure, position, and overall intensity relative to the primary core lines, is striking.

To interpret our resonant Auger data, we first elucidate the different electronic transitions studied and their relevance to the materials' solid-state electronic structure. Figure 2(a) shows Ti K-edge XAS spectra for single-crystal $SrTiO_3$. The data are plotted for different sample geometries relative to the incident synchrotron-beam wave vector $\boldsymbol{q}$ and synchrotron-beam polarization vector $\boldsymbol{e}$. As demonstrated by their sensitivity to sample geometry [48], the first two peaks of the spectra are dipole-forbidden transitions of the Ti 1s electron to the crystal-field split Ti 3d t_{2g} (d_{xy}, d_{yz}, and d_{zx}) and Ti 3d e_g ($d_{3z^2-r^2}$, and $d_{x^2-y^2}$) unoccupied molecular orbitals of octahedral (O_h) symmetry. These peaks are followed by a broad, double-humped maximum that is not polarization dependent; this structure arises from electronic transitions of the Ti 1s electron to the Ti 3d orbitals on the next-nearest-neighbor (NNN) Ti atoms via local Ti 4p-O 2p-NNN Ti 3d hybridization (i.e., band-structure effects) [49,50]. The fact that these transitions are dipole allowed and contribute such
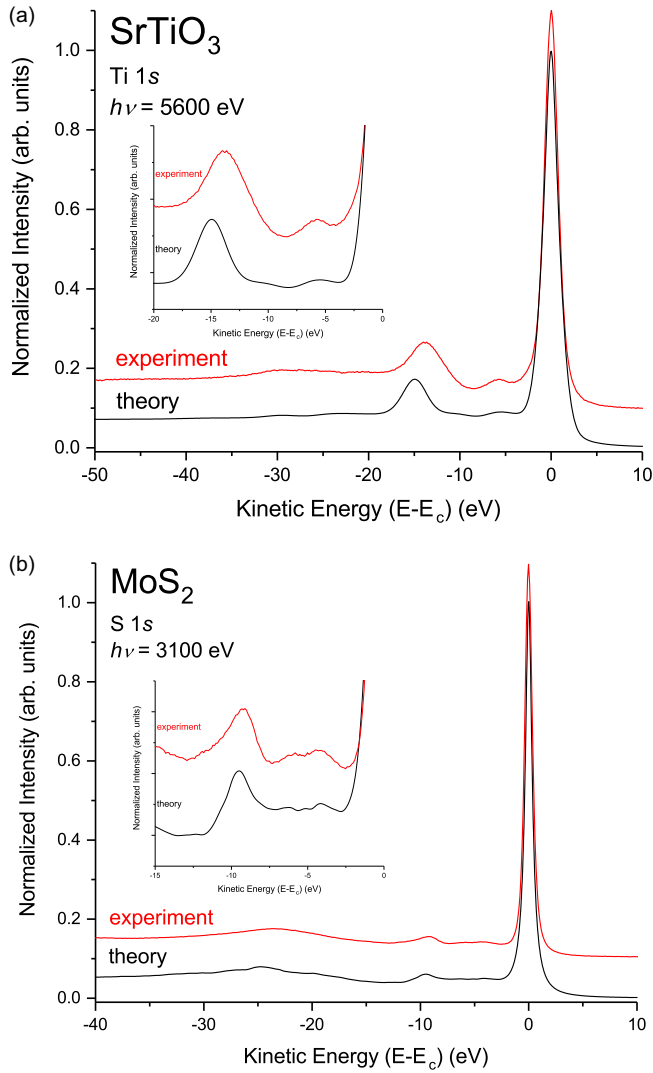
FIG. 1. (a) Calculated Ti $1s$ XPS spectrum for SrTiO$_3$ and experiment. (b) Calculated S $1s$ XPS spectrum for MoS$_2$ and experiment. The insets show expanded views of the satellite-loss structures. The spectra have been normalized to unit peak height and offset for clarity.

FIG. 2. (a) Calculated Ti $1s$ XAS spectrum for SrTiO$_3$ and experiment. (b) Calculated S $1s$ XAS spectrum for MoS$_2$ and experiment. Bottom: Noninteracting theory. Lower middle: Interacting-BSE theory. Upper middle: BSE + cumulant. Top: Experiment. The spectra have been normalized to unit step height and offset for clarity.

small intensity to the absorption spectra demonstrates that most of their character originates from the neighboring metal-ion 3d states. Further analysis shows that they are dominated by Ti 3d e_g rather than Ti 3d t_{2g} transitions on account of the larger overlap of σ versus π bonding. Note that these features lie well below the main Ti $1s \rightarrow 4p$ absorption edge that occurs at 4984 eV in SrTiO$_3$.

Likewise, Fig. 2(b) shows S K-edge XAS spectra for MoS$_2$. The data are plotted for the synchrotron-beam wave vector **q** aligned at glancing (80°) and normal (0°) incidence relative to the MoS$_2$ c-axis. The intense dipole allowed S $1s \rightarrow 3p^*$ transition shows strong polarization dependence on account of the quasi-two-dimensional crystal structure of MoS$_2$ in addition to the Mo D_{3h} molecular-point-group symmetry that is atypical for sixfold coordinated transition-metal complexes [51].

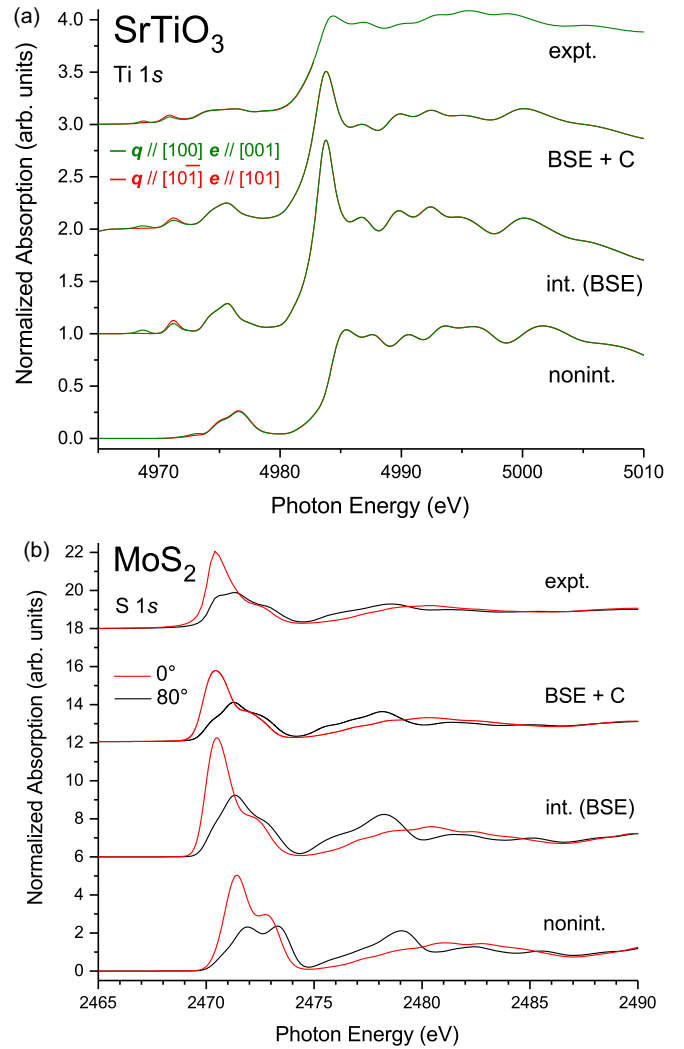Compared to the data are theoretical calculations of the Ti K-edge XAS for SrTiO$_3$ and the S K-edge XAS for MoS$_2$

following earlier studies [27,36] and solution of the BSE [38]. To determine the excitonic contributions to the absorption spectra, the calculations were repeated, but with the electron–core hole-interaction terms omitted. It is clear from the interacting versus noninteracting spectra that the onset of the Ti K edge contains significant excitonic enhancement. The Ti 3d levels are pulled down in energy by 2.6 eV, and they are significantly split off from both the local and nonlocal dipole transitions, consistent with the fact that the Ti 3d electrons lie closer to the nucleus than the Ti 4s and Ti 4p levels [26]. We also note that the BSE calculation significantly overestimates the intensity of the signature Ti $1s \rightarrow 4p$ edge. The theory also fails to predict the filling of the trough that follows the Ti $1s \rightarrow$ NNN 3d region of the spectra, in addition to the filling of the two large troughs at the satellite binding energies roughly 6 eV and 14 eV above the main Ti $1s \rightarrow 4p$ edge. Likewise, for MoS$_2$, theory and experiment show disparity in the intensity of the signature edge; however, the edge is

pulled down now by only 0.47 eV, and there is less excitonic enhancement throughout the spectra.

Although the BSE result accounts for the Coulomb interaction between the core hole and the photoexcited electron, it is incomplete because it does not account for many-electron shake-up excitations. However, following Refs. [29–31,52], these excitations may be included by convolving the BSE spectrum $\mu'(\omega)$ with the photon-energy dependent spectral function $A(\omega,\omega')$ according to

$$\mu(\omega) = \int d\omega' A(\omega, \omega') \mu'(\omega - \omega'). \quad (2)$$

As described above, the photon-energy dependence of $A(\omega,\omega')$ arises from the interaction of the valence electrons with the photoelectron (extrinsic interactions), as well as the interference between the photoelectron and core hole-mediated excitations. (For example, the cross section for a satellite is expected to be smaller for the Ti $1s \rightarrow 3d$ transition relative to the Ti $1s \rightarrow 4p$ transition because the former leaves a localized electron in the Ti $3d$ level that would more completely screen the core hole.) Previously, the photon-energy dependence in the spectral function was modeled using a simple parametrization form for such interference [42]. That model for the interference, however, was based on free electrons interacting with plasmons, and it is more appropriate for metals and plasmonlike excitations. Here, we simply replace the photon-energy dependent spectral function with a photon-energy independent core hole-spectral function alone, with extrinsic and interference effects neglected; i.e., we make the approximation $A(\omega, \omega') = A(\omega')$ in Eq. (2) and calculate the spectral function using the RT-TDDFT cumulant approach [16].

For SrTiO$_3$, large differences are observed between the convolved and non-convolved spectra because of the relatively large satellite intensity observed. The intensity of the Ti $1s \rightarrow 4p$ transition is reduced and redistributed to higher photon energies, and this redistribution occurs primarily at the satellite binding energies. Note as well the filling of the trough 5 eV above the Ti $1s \rightarrow$ NNN $3d$ feature. Likewise, significant changes are observed between the MoS$_2$ spectra. Despite the above simplification, agreement between theory and experiment is greatly improved for both SrTiO$_3$ and MoS$_2$.

In order to investigate the nature of the satellite excitations, we now turn to our resonant Auger data. Although the resonant Auger effect was originally studied in noble gases [53], it has found significant utility in solid-state physics, having been employed to study excitonic effects in graphite [54] and other solids [55–59], including MoS$_2$ [27,60].

Figure 3(a) shows the Ti K-$L_{2,3}L_{2,3}(^1D_2)$ Auger spectrum recorded with photon energy set to the Ti $1s \rightarrow 3d\ t_{2g}$ quadrupolar transition, to the first maximum of the Ti $1s \rightarrow$ NNN $3d$ dipole transition, and to the Ti $1s \rightarrow 4p$ dipole transition, as indicated. Note the 2-eV shift of the Auger peak to higher kinetic energy when the photon energy is set to the energy of the Ti $1s \rightarrow 3d\ t_{2g}$ transition. This shift demonstrates the localized nature of the Ti $3d$ states and the large amount of core hole screening they produce. On the other hand, the strong intersite hybridization of the two dipole-allowed transitions delocalizes the photoelectron, leaving little or no
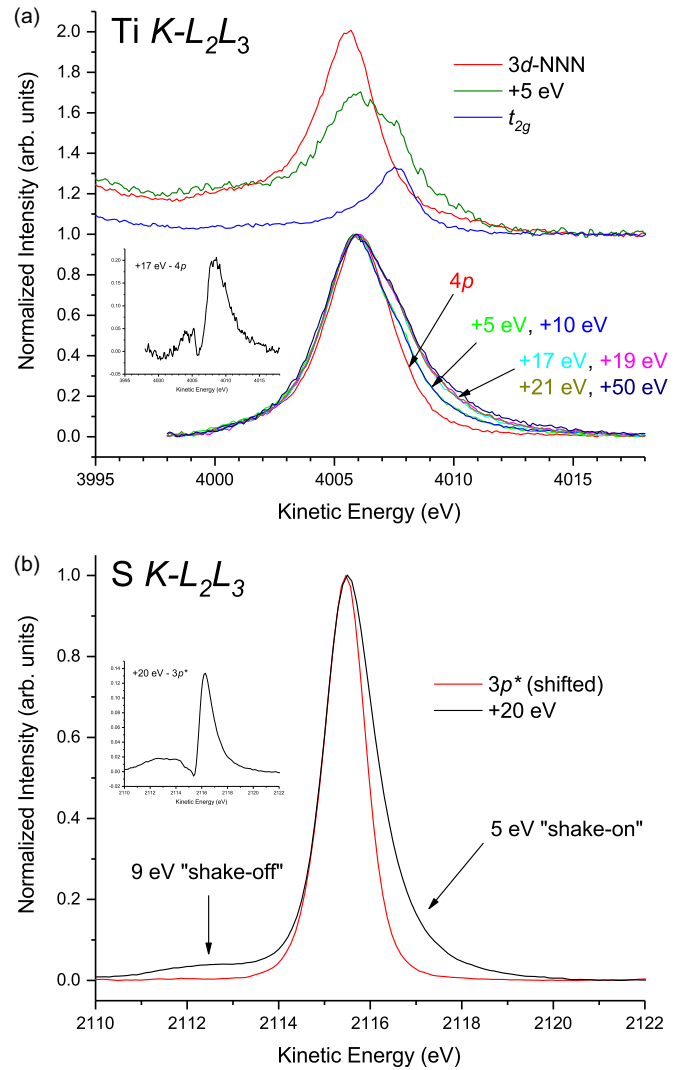

FIG. 3. (a) Ti K-$L_{2,3}L_{2,3}(^1D_2)$ Auger spectrum for SrTiO$_3$ recorded at different photon energies around the Ti K edge. Top: At the Ti $1s \rightarrow$ NNN $3d$ transition, 5 eV above it, and at the Ti $1s \rightarrow 3d\ t_{2g}$ transition. The data have been normalized to the background above the Auger peak. Bottom: At the Ti $1s \rightarrow 4p$ transition and with excess photon energy as indicated. The data have been normalized to equal peak height and have had a Shirley background removed. The inset shows the difference between the spectra recorded at the Ti $1s \rightarrow 4p$ transition and 17 eV above it. (b) S K-$L_{2,3}L_{2,3}(^1D_2)$ Auger spectrum for MoS$_2$ recorded at the S $1s \rightarrow 3p^*$ resonance and 20 eV above it. The data have been normalized to equal peak height and have had a Shirley background removed. The spectrum recorded at resonance has been shifted by -0.33-eV kinetic energy. The inset shows their difference.

spectator-electron density on the absorbing atom with which to screen the core hole.

Turning to MoS$_2$, Fig. 3(b) shows the S K-$L_{2,3}L_{2,3}(^1D_2)$ Auger spectrum recorded with photon energy set to the S $1s \rightarrow 3p^*$ resonance and 20 eV above it. Again, a shift of the Auger peak to higher kinetic energy is observed at threshold, but this shift is now only 0.3 eV (it has been shifted to lower kinetic energy by 0.33 eV in the figure).
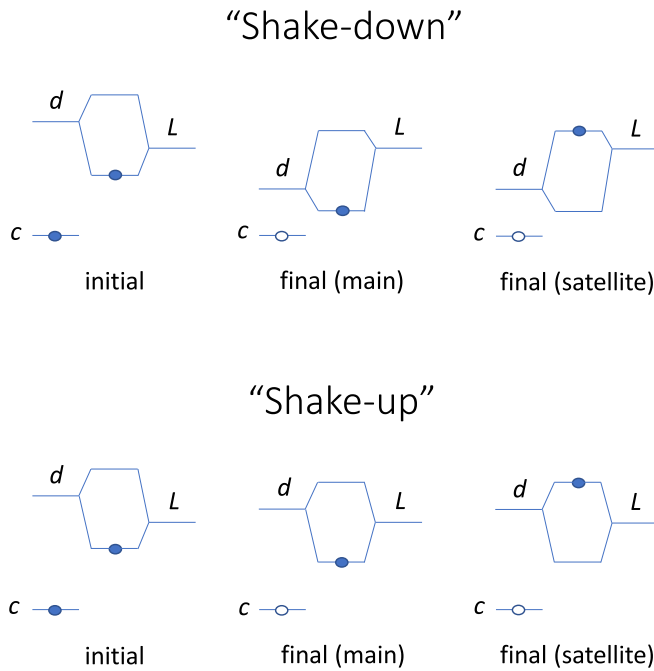
"Shake-down"

"Shake-up"

FIG. 4. Illustration of shake-down and shake-up charge-transfer processes following core photoionization (see text).

As discussed by Armen *et al.* [33], the shift of the Auger peak at resonance gives a direct measure of the energy required to liberate the excited photoelectron from its final ionic state. As in the case of an optical transition, this energy may be interpreted as the excitonic or Coulomb binding energy of the core-to-valence transition. Consequently, for both materials, we conclude that the pulling down of the conduction-band states by the core hole potential does not exceed the materials' band gap (the band gap of $SrTiO_3$ is 3.2 eV [28] and the band gap of MoS_2 is 1.3 eV [61]). These observations are consistent with the BSE solutions of Fig. 2 as well as with the large-supercell calculations of Yamamoto *et al.* [26].

With an eye on what is to follow, we now detail the different shake processes possible in a solid. Lee, Gunnarsson, and Hedin [62] considered charge-transfer excitations for a three-level solid-state system consisting of a deep core level, a ligand level, and a less tightly bound metal level. In the ground state, the core level and the ligand level are occupied. (This model should be applicable to $SrTiO_3$, which has a large amount of covalency [63].) The ground state of the photoionized atom will always possess more valence charge than the ground state of the neutral system because the core hole lowers the energy of its valence levels. As Fig. 4 illustrates, two situations can then arise. In the first, the creation of the core hole pulls the metal level below the ligand level, and, consequently, there is a nonzero probability that the outer electron will not stay on the ligand atom, but it will be transferred to the metal atom. The photoemission then has a leading "shake-down" peak, and its satellite reflects the process where the electron is not transferred, but, rather, it stays on the ligand atom. In the second, the metal and ligand levels do not cross, and the lowest final state has the electron remaining on the ligand atom. The satellite in this case is referred to as "shake-up," and it corresponds to the

transfer of the electron from the ligand to the metal atom. Our observed shift of the Auger peak at threshold suggests that the $SrTiO_3$ satellites are charge-transfer shake-up excitations, because the metal and ligand levels apparently do not cross during photoionization.

To explore the electrostatic nature of the satellites and to further address the energetics of well-screened and unscreened photopeaks, we turn to our Auger data recorded with excess photon energy above threshold. These data are also shown in Fig. 3. Unlike the case of Ar gas that can only have electron shake-up or shake-off, additional intensity appears on the *high* kinetic-energy side of the main Ti Auger peak, whereas it appears only on the *low* kinetic-energy side for Ar gas [22]. This additional intensity in the Ti Auger spectrum turns on for photon energies equaling the satellite binding energies above both the Ti $1s \rightarrow$ NNN $3d$ and the Ti $1s \rightarrow 4p$ transitions; it also has similar kinetic energy as the resonant Auger peak when the photon energy is set to the Ti $1s \rightarrow 3d$ transition, i.e., when the Ti $1s$ electron is promoted directly to the Ti $3d$ level. These observations experimentally identify the $SrTiO_3$ satellites as ligand-to-metal charge-transfer shake-up, because their turn-on occurs at the satellite binding energies, and they produce the same amount of core hole screening as the Ti $1s$ electron when it is promoted to and localized in the Ti $3d$ level [45].

Unlike the case of $SrTiO_3$, the main S Auger peak sports additional intensity on both its high and low kinetic-energy sides. The skew or "tailing" of the Auger peak to high kinetic energy turns on within 5 eV of the S $1s \rightarrow 3p^*$ edge. The fact that the satellites appear triply split in the S $1s$ XPS spectrum is consistent with the added complexity of the Mo D_{3h} molecular-point-group symmetry that splits the Mo $4d$ orbitals into three sets: A_1' ($4d_{3z^2-r^2}$), E' ($4d_{xy}$ and $4d_{x^2-y^2}$), and E'' ($4d_{xz}$ and $4d_{yz}$) [64]. We therefore conclude that charge-transfer screening from the neighboring Mo atoms is the origin of the low energy satellite structure of the S $1s$ XPS spectrum.

To examine more closely the photon-energy dependence of the 9-eV MoS_2 satellite, Fig. 5(a) shows an expanded view of the low kinetic-energy side of the S Auger peak recorded in approximately 0.5-eV photon-energy increments above the S $1s \rightarrow 3p^*$ resonance. The satellite first appears 8 eV above resonance. It reaches its maximum intensity by 11 eV, decreases to zero by 14 eV, and then, remarkably, grows again. Analogous to the satellite found in Ar gas [22], we liken this excitation to a shake-off charge-transfer process, consistent with the formal closed-shell S $3p^6$ orbitals and the appearance of this peak on the low kinetic-energy side of the main S Auger line. (Simple electron counting gives Mo a formal +4 ionic charge leading to $Mo^{4+} 4d^2$ and $S^{2-} 3p^6$ configurations.)

Figure 5(b) compares the intensity of this peak, the intensity of the main S Auger line, and the intensity of the entire S K-$L_{2,3}L_{2,3}$ Auger spectrum as a function of photon energy. The satellite intensity follows the total XAS curve, but it is shifted upwards in energy, confirming the ansatz of Stern *et al.*: "The dipole sum rule states that the total absorption must remain the same independent of multielectron effects. The photo-electron can still have EXAFS associated with it, but the EXAFS will be shifted to higher energy" [32]. Note the blurring of the total XAS relative to the isolated
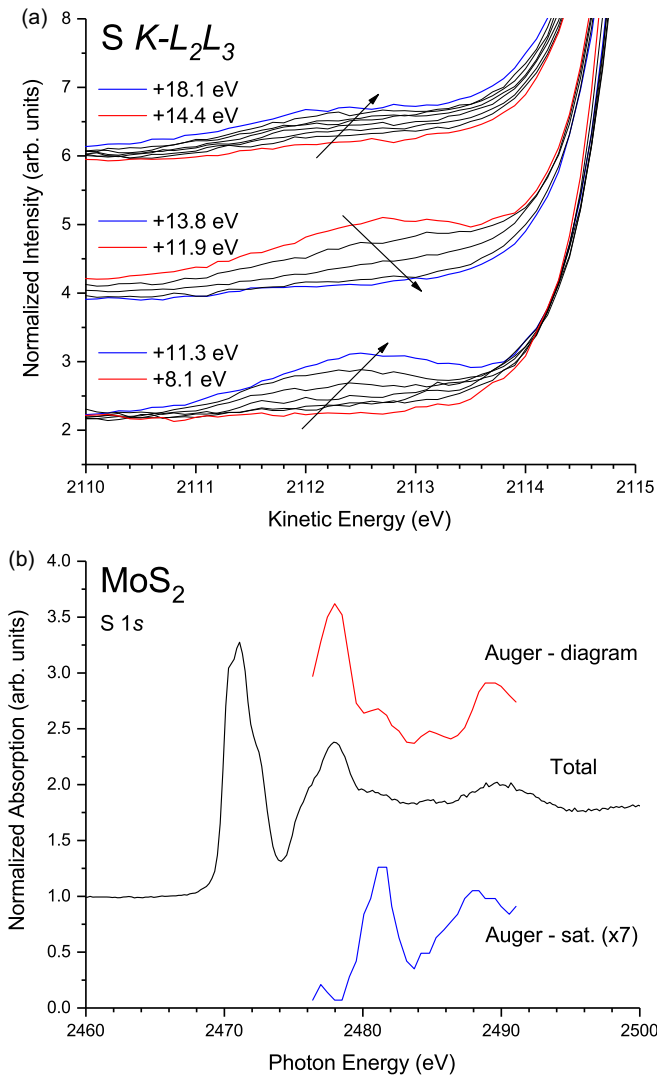
FIG. 5. (a) Expanded view of the low-kinetic-energy satellite contribution to the S K-$L_{2,3}L_{2,3}$($^1D_2$) Auger spectrum for MoS_2 recorded in approximately 0.5-eV photon-energy increments above the S $1s \rightarrow 3p^*$ resonance as indicated. The data have been offset for clarity and normalized to the background above the Auger peak. The arrows indicate the effect of increasing photon energy. (b) Decomposition of the S K-$L_{2,3}L_{2,3}$($^1D_2$) Auger decay as a function of photon energy around the S K edge. Top: Diagram Auger decay. Middle: Total Auger decay (standard XAS). Bottom: Satellite Auger decay. The spectra have been offset for clarity.

FIG. 6. (a) Theoretical time dependence of the total Bader charge on the photon-absorbing Ti atom, its six near-neighbor O atoms, and their sum for $SrTiO_3$. (b) Theoretical time dependence of the total Bader charge on the photon-absorbing S atom, its three near-neighbor Mo atoms, and their sum for MoS_2. The plots begin at time $t = 0$, i.e., the creation of the core hole. The charge is referenced to the ground-state charge Q_0 around the photon-absorbing atom and its near neighbors (NN). It is displayed in positive-electron units.

intensity of the main S Auger line that is the origin of the many-body reduction factor S_0^2 in extended x-ray-absorption fine-structure (EXAFS) analysis [65].

In order to analyze the time evolution of the many-body system, Bader analysis [66–70] was performed to obtain the atomic charges relative to the ground state $Q(t) - Q_0$ for the photon-absorbing atom, as well as for its near neighbors. As can be seen in Fig. 6(a) for $SrTiO_3$, there are several time scales involved. In the first fraction of 1 fs, electrons flood from the six neighboring O atoms (and other surrounding atoms) onto the absorbing Ti atom to screen the core hole. By approximately 0.13 fs, the absorbing Ti atom reaches a net-screening charge of nearly two electrons, and, from that
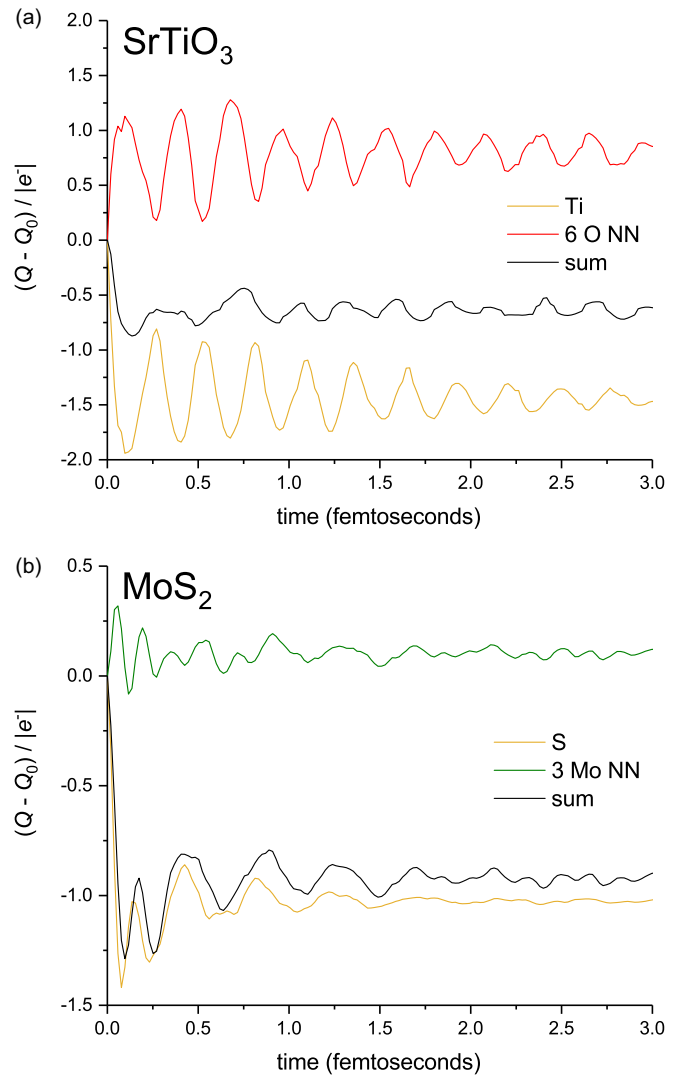
time on, charge oscillates between the Ti atom and its six O neighbors, with a frequency corresponding to the high energy satellite in the XPS. The charge oscillations range from about 2.0 to 1.0 electron on the Ti atom, and from approximately -0.5 to -1.5 electrons on the O atoms. It is clear from the sum $Q_{total}(t) = Q_{Ti}(t) + Q_O(t)$ that a significant amount of the charge oscillation occurs within the Ti-O octahedron. On the other hand, lower frequency oscillations, as well as about half of the zero-frequency component (corresponding to the main-line density), persist in the sum, indicating that these are longer range excitations, coming from next-nearest neighbors and beyond.

Formally, the oscillations observed arise from the classic time evolution of $\Psi(N - 1)$ that is determined by the
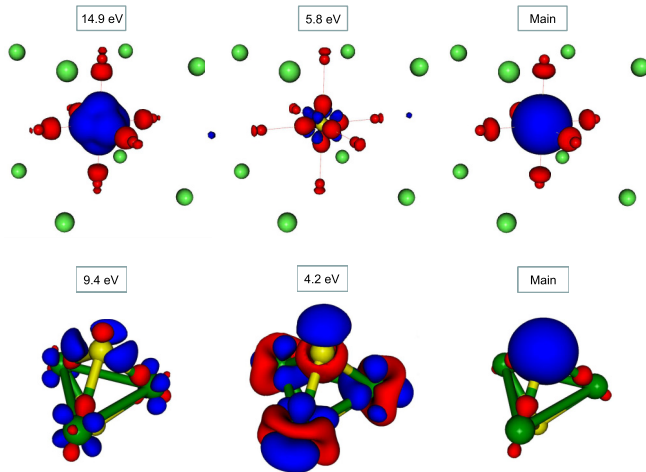
FIG. 7. Theoretical excited-state electron-density fluctuations $\Delta\rho(\mathbf{r}, \omega_{\text{sat}})$ calculated at frequencies corresponding to the satellite binding energies and the main line as indicated. Top: $SrTiO_3$. Bottom: MoS_2. Red indicates negative-electron density and blue indicates positive-electron density, as determined by our resonant Auger measurements (see text). The density fluctuation reflecting the zero frequency is shown as a difference with respect to the ground state, whereas those reflecting the satellite peaks are shown as differences with respect to the main-line density.

eigenstates of $H'(N - 1)$ in Eq. (1) and their time and energy dependent phase factors $e^{-iE_n t/\hbar}$. This solution of Schrödinger's equation renders charge-density oscillations with frequencies $\omega_{fi} = (E_f - E_i)/\hbar$ [10]. It also explains the experimental result that positive work is required to transfer an electron from the six O neighbors to the Ti atom: The net-screening charge on the Ti atom increases from one to two electrons at the time of the measurement whereupon energy must be conserved. Fig. 6(b) shows a similar result for MoS_2. Again, charge rushes in to screen the core hole at $t = 0$, but longer-range excitations are seen to play a more significant role for this material due, in part, to the positive charge on the Mo atoms in the ground state and its larger dielectric constant (13.5 for MoS_2 and 5.06 for $SrTiO_3$).

To explore the physical nature of the satellites in real space, Fig. 7(a) shows the excited-state electron-density fluctuations $\Delta\rho(\mathbf{r}, \omega_{\text{sat}})$ for $SrTiO_3$ calculated at frequencies corresponding to 14.9, 5.8, and 0 eV (i.e., the main core line). The high energy satellite has the same shape as the e_g molecular orbitals of the $[TiO_6]^{8-}$ cluster [71], confirming the experimental assignment that this transition is ligand O $2p_\sigma$ to metal Ti $3d$ e_g charge transfer [45]. Note the O s-p hybridization that orients the charge density of the O $2p_\sigma$ orbitals towards the Ti atom [72]. The low energy satellite, on the other hand, shows a much more complicated density fluctuation. Observed are transitions between the O $2p_\pi$ orbitals and the metal $3d$ t_{2g} orbitals [73]. However, unique to this transition is charge that flows back to the O ligands. Such π back-bonding is a common occurrence in organic chemistry [74], but here it is observed in reverse through the e_g channel on account of the π excitation and the much larger overlap of the O $2p_\sigma$ and Ti $3d$ e_g orbitals. We note that the sum of the Ti and O densities of Fig. 6(a) reflects the lower frequency of this exci-

tation, indicating that it more closely couples to the medium than the higher energy excitation, while the zero-frequency excitation uniformly fills the Ti $3d$ t_{2g} and e_g orbitals resulting in a spherical-charge density around the Ti atom by Unsöld's theorem. The filling of charge around the Ti atom is consistent with the t_{2g} and e_g oscillations being driven in phase at zero frequency and the shake-up illustration in Fig. 4.

Figure 7(b) shows the excited-state electron-density fluctuations for MoS_2. The high energy satellite is again much "cleaner," reflecting its more localized nature. We note the red S sp and the blue S sp^2 hybrid orbitals that overlap the blue and red Mo $4d$ orbitals of appropriate symmetry. These orbitals closely resemble the upper valence-band states (red S and red Mo) and the lower conduction-band states (blue S and blue Mo) of MoS_2 [75], further identifying this transition as shake-off charge transfer. Note that extra energy is required to promote the S $3p$ shake electron across the band gap due to the additional Coulomb attraction of the doubly photoionized S atom. The translational symmetry of the crystal is broken by the core hole potential, but the local C_{3v} site symmetry around the S atoms is preserved. Furthermore, charge is transferred back to the S atom from the Mo orbitals, consistent with the backflow observed for $SrTiO_3$ and calculations of the Born effective charge and π back-bonding in MoS_2 [76]. The lower energy excitation shows reversal of electron density on the S and Mo orbitals in addition to changes in their hybridization that is consistent with the prediction of earlier models [77] and the splitting off from the band edges of the Mo d_{xz} and d_{yz} orbitals [78]. The zero-frequency excitation again shows a symmetrical filling of charge around the photon-absorbing S atom.

Counter to previous theoretical assignments of well-screened and unscreened photopeaks, our data demonstrate that the main peak and satellite correspond to screened and overscreened states: The experimentally observed charge-transfer screening occurs with higher energy than the main- or primary-photoemission peak, and this result likely arises from competition between the long-range screening that occurs in a solid and the short-range charge-transfer screening that occurs between atoms. While this result may seem surprising, it is in the same spirit as the observation that the lowering of the conduction-band states on the photon-absorbing atom by the core hole potential does not exceed the materials' band gap. The appearance of satellites on both sides of the S Auger peak further witnesses the complexity of core hole-induced valence excitations in a solid.

V. CONCLUSIONS

We have presented a comparative study of the XPS and XAS spectra of $SrTiO_3$ and MoS_2. Noteworthy agreement is obtained by combining first-principles calculations utilizing RT-TDDFT for the cumulant representation of the core hole Green's function with the BSE in order to include both excitonic and multielectron effects: The accuracy of the cumulant was demonstrated *a priori* by XPS and applied *a posteriori* to the BSE treatment of the XAS. Resonant Auger-electron spectroscopy assigns the loss structures in $SrTiO_3$ as ligand-to-metal charge transfer, while for MoS_2 it identifies both "shake-on" and shake-off charge-transfer excitations. The S shake-off excitation turns on with excess photon energy above

the S K edge that significantly exceeds the band gap because of the additional Coulomb cost of multiple ionization, and its photon-energy dependence validates the dipole sum rule for shake satellites that is harmonious with the insight of Stern *et al.* [32]. The atomic charges and excited-state electron-density fluctuations are found to reflect materials' solid-state electronic structure, loss of translational symmetry around the core hole, and breakdown of the sudden approximation. They also demonstrate the competition between long- and short-range screening that occurs in a solid.

[1] T. A. Carlson, *Photoelectron and Auger Spectroscopy* (Plenum, New York, 1975).

[2] K. Siegbahn, C. Nordling, G. Johansson, J. Hedman, P. H. Hedén, K. Hamrin, U. Gelius, T. Bergmark, L. O. Werme, R. Manne, and Y. Baer, *ESCA Applied to Free Molecules* (North-Holland, Amsterdam, 1969).

[3] T. A. Carlson, M. O. Krause, and W. E. Moddeman, J. Phys. (Paris) **32**, C4 (1971).

[4] K. S. Kim and R. E. Davis, J. Electron Spectrosc. Relat. Phenom. **1**, 251 (1972).

[5] K. S. Kim and J. Electron, Spectrosc. Relat. Phenom. **3**, 217 (1974).

[6] K. S. Kim, Phys. Rev. B **11**, 2177 (1975).

[7] T. Åberg, Phys. Rev. **156**, 35 (1967).

[8] R. Manne and T. Åberg, Chem. Phys. Lett. **7**, 282 (1970).

[9] H. W. Meldner and J. D. Perez, Phys. Rev. A **4**, 1388 (1971).

[10] L. I. Schiff, *Quantum Mechanics*, 3rd ed. (McGraw-Hill, New York, 1968).

[11] A. Fujimori, F. Minami, and S. Sugano, Phys. Rev. B **29**, 5225(R) (1984).

[12] A. Fujimori and F. Minami, Phys. Rev. B **30**, 957 (1984).

[13] M. A. van Veenendaal and G. A. Sawatzky, Phys. Rev. Lett. **70**, 2459 (1993).

[14] M. W. Haverkort, M. Zwierzycki, and O. K. Andersen, Phys. Rev. B **85**, 165113 (2012).

[15] M. Taguchi, M. Matsunami, Y. Ishida, R. Eguchi, A. Chainani, Y. Takata, M. Yabashi, K. Tamasaku, Y. Nishino, T. Ishikawa, Y. Senba, H. Ohashi, and S. Shin, Phys. Rev. Lett. **100**, 206401 (2008).

[16] J. J. Kas, F. D. Vila, J. J. Rehr, and S. A. Chambers, Phys. Rev. B **91**, 121112(R) (2015).

[17] F. Borgatti, J. A. Berger, D. Céolin, J. S. Zhou, J. J. Kas, M. Guzzo, C. F. McConville, F. Offi, G. Panaccione, A. Regoutz, D. J. Payne, J.-P. Rueff, O. Bierwagen, M. E. White, J. S. Speck, M. Gatti, and R. G. Egdell, Phys. Rev. B **97**, 155102 (2018).

[18] M. Guzzo, G. Lani, F. Sottile, P. Romaniello, M. Gatti, J. J. Kas, J. J. Rehr, M. G. Silly, F. Sirotti, and L. Reining, Phys. Rev. Lett. **107**, 166401 (2011).

[19] J. S. Zhou, J. J. Kas, L. Sponza, I. Reshetnyak, M. Guzzo, C. Giorgetti, M. Gatti, F. Sottile, J. J. Rehr, and L. Reining, J. Chem. Phys. **143**, 184109 (2015).

[20] L. Hedin, in *Solid-State Photoemission and Related Methods: Theory and Experiment*, edited by W. Schattke and M. A. Van Hove (Wiley, New York, 2003).

[21] A. Fahlman, K. Hamrin, R. Nordberg, C. Nordling, and K. Siegbahn, Phys. Lett. **20**, 159 (1966).

[22] T. LeBrun, S. H. Southworth, G. B. Armen, M. A. MacDonald, and Y. Azuma, Phys. Rev. A **60**, 4667 (1999).

[23] G. B. Armen, T. Åberg, K. R. Karim, J. C. Levin, and B. Crasemann, Phys. Rev. Lett. **54**, 182 (1985).

[24] F. Heiser, S. B. Whitfield, J. Viefhaus, U. Becker, P. A. Heimann, and D. A. Shirley, J. Phys. B **27**, 19 (1994).

[25] E. L. Shirley, Phys. Rev. Lett. **80**, 794 (1998).

[26] T. Yamamoto, T. Mizoguchi, and I. Tanaka, Phys. Rev. B **71**, 245113 (2005). Large supercell DFT band-structure calculations shown in Figs. 1 and 3 of this reference find the Ti $1s$ core hole potential pulls the Ti $3d$ level down by 2.3 eV and the Ti $4p$ level down by 0.7 eV using the nomenclature of Ref. [46] which finds $U_{dc} = 6.0$ eV from a TiO_6 cluster-model analysis. The DFT band-structure values are close to the present BSE results for which the "pulling down" values are instead 2.6 eV and 0.9 eV.

[27] J. C. Woicik, C. Weiland, A. K. Rumaiz, M. Brumbach, N. F. Quackenbush, J. M. Ablett, and E. L. Shirley, Phys. Rev. B **98**, 115149 (2018).

[28] L. Sponza, V. Véniard, F. Sottile, C. Giorgetti, and L. Reining, Phys. Rev. B **87**, 235102 (2013).

[29] P. Nozières and C. T. de Dominicis, Phys. Rev. **178**, 1097 (1969).

[30] M. Calandra, J. P. Rueff, C. Gougoussis, D. Céolin, M. Gorgoi, S. Benedetti, P. Torelli, A. Shukla, D. Chandesris, and C. Brouder, Phys. Rev. B **86**, 165102 (2012).

[31] E. Klevak, J. J. Kas, and J. J. Rehr, Phys. Rev. B **89**, 085123 (2014).

[32] E. A. Stern, B. A. Bunker, and S. M. Heald, Phys. Rev. B **21**, 5521 (1980).

[33] G. B. Armen, H. Aksela, T. Åberg, and S. Aksela, J. Phys. B **33**, R49 (2000).

[34] D. A. Shirley, Phys. Rev. B **5**, 4709 (1972).

[35] J. C. Woicik, E. L. Shirley, C. S. Hellberg, K. E. Andersen, S. Sambasivan, D. A. Fischer, B. D. Chapman, E.A. Stern, P. Ryan, D. L. Ederer, and H. Li, Phys. Rev. B **75**, 140103(R) (2007).

[36] E. Cockayne, E. L. Shirley, B. Ravel, and J. C. Woicik, Phys. Rev. B **98**, 014111 (2018).

[37] P. A. Young, J. Phys. D **1**, 936 (1968).

[38] K. Gilmore, J. Vinson, E. L. Shirley, D. Prendergast, C. D. Pemmaraju, J. J. Kas, F. D. Vila, and J. J. Rehr, Comp. Phys. Comm. **197**, 109 (2015).

[39] The resolution of the double-crystal Si(220) monochromator is estimated to be 0.33 eV at the Ti K edge, and the resolution

of the double-crystal Si(111) monochromator is estimated to be 0.22 eV at the S K edge.

[40] E. L. Shirley, Radiat. Phys. Chem. **167**, 108165 (2020).

[41] M. O. Krause and J. H. Oliver, J. Phys. Chem. Ref. Data **8**, 329 (1979). The lifetime-Lorentzian width is estimated to be 0.94 eV for the Ti 1s core and 0.59 eV for the S 1s core.

[42] J. J. Kas, J. J. Rehr, and J. B. Curtis, Phys. Rev. B **94**, 035156 (2016).

[43] C. Weiland, A. K. Rumaiz, P. Lysaght, B. Karlin, J. C. Woicik, and D. A. Fischer, J. Electron. Spectrosc. Relat. Phenom. **190**, 193 (2013).

[44] C. Weiland, C. Jaye, N. F. Quackenbush, E. Gann, Z. Fu, J. P. Kirkland, B. A. Karlin, B. Ravel, J. C. Woicik, and D. A. Fischer, Synchrotron Radiat. News **31**, 23 (2018).

[45] J. C. Woicik, C. Weiland, and A. K. Rumaiz, Phys. Rev. B **91**, 201412(R) (2015).

[46] K. Okada and A. Kotani, J. Electron Spectrosc. Relat. Phenom. **62**, 131 (1993).

[47] A. E. Bocquet, T. Mizokawa, K. Morikawa, A. Fujimori, S. R. Barman, K. Maiti, D. D. Sarma, Y. Tokura, and M. Onoda, Phys. Rev. B **53**, 1161 (1996).

[48] C. Brouder, J. Phys.: Condens. Matter **2**, 701 (1990).

[49] R. V. Vedrinskii, V. L. Kraizman, A. A. Novakovich, Ph. V. Demekhim, and S. V. Urazhdin, J. Phys. Condens. Matter **10**, 9561 (1998).

[50] Z. Y. Wu, D. C. Xian, T. D. Hu, Y. N. Xie, Y. Tao, C. R. Natoli, E. Paris, and A. Marcelli, Phys. Rev. B **70**, 033104 (2004).

[51] F. A. Cotton, *Chemical Applications of Group Theory*, 2nd ed. (Wiley, New York, 1971).

[52] L. Campbell, L. Hedin, J. J. Rehr, and W. Bardyszewski, Phys. Rev. B **65**, 064107 (2002).

[53] G. S. Brown, M. H. Chen, B. Crasemann, and G. E. Ice, Phys. Rev. Lett. **45**, 1937 (1980).

[54] P. A. Brühwiler, A. J. Maxwell, C. Puglia, A. Nilsson, S. Andersson, and N. Mårtensson, Phys. Rev. Lett. **74**, 614 (1995).

[55] H. Wang, J. C. Woicik, T. Åberg, M. H. Chen, A. Herrera-Gomez, T. Kendelewicz, A. Mäntykenttä, K. E. Miyano, S. Southworth, and B. Crasemann, Phys. Rev. A **50**, 1359 (1994).

[56] W. Drube, R. Treusch, and G. Materlik, Phys. Rev. Lett. **74**, 42 (1995).

[57] A. Fölisch, O. Karis, M. Weinelt, J. Hasselström, A. Nilsson, and N. Mårtensson, Phys. Rev. Lett. **88**, 027601 (2001).

[58] J. Danger, P. Le Fèvre, H. Magnan, D. Chandesris, S. Bourgeois, J. Jupille, T. Eickhoff, and W. Drube, Phys. Rev. Lett. **88**, 243001 (2002).

[59] J. C. Woicik, J. M. Ablett, N. F. Quackenbush, A. K. Rumaiz, C. Weiland, T. C. Droubay, and S. A. Chambers, Phys. Rev. B **97**, 245142 (2018).

[60] T. A. Sasaki, Y. Baba, K. Yoshii, and H. Yamamoto, J. Electron Spectrosc. Relat. Phenom. **76**, 411 (1995).

[61] *Gmelin Handbook of Inorganic and Organometallic Chemistry*, 8th ed. (Springer-Verlag, Berlin, 1995), Vol. B7.

[62] J. D. Lee, O. Gunnarsson, and L. Hedin, Phys. Rev. B **60**, 8034 (1999).

[63] K. Okada, T. Uozumi, and A. Kotani, J. Phys. Soc. Jpn. **63**, 3176 (1994).

[64] E. I. Stiefel, R. Eisenberg, R. C. Rosenberg, and H. B. Gray, J. Am. Chem. Soc. **88**, 2956 (1966).

[65] J. J. Rehr, E. A. Stern, R. L. Martin, and E. R. Davidson, Phys. Rev. B **17**, 560 (1978).

[66] W. Tang, E. Sanville, and G. Henkelman, J. Phys.: Condens. Matter **21**, 084204 (2009).

[67] E. Sanville, S. D. Kenny, R. Smith, and G. Henkelman, J. Comp. Chem. **28**, 899 (2007).

[68] G. Henkelman, A. Arnaldsson, and H. Jónsson, Comput. Mater. Sci. **36**, 354 (2006).

[69] M. Yu and D. R. Trinkle, J. Chem. Phys. **134**, 064111 (2011).

[70] R. Bader, *Atoms in Molecules: A Quantum Theory* (Oxford University, New York, 1990).

[71] M. Karplus and R. N. Porter, *Atoms and Molecules* (Benjamin, New York, 1970), Chap. 6.4.

[72] J. C. Woicik, E. J. Nelson, L. Kronik, M. Jain, J. R. Chelikowsky, D. Heskett, L. E. Berman, and G. S. Herman, Phys. Rev. Lett. **89**, 077401 (2002).

[73] The O 2p orbitals appear as red annuli because the sum of the p_x and p_y probability densities has no azimuthal dependence and is zero along the z direction. Similarly, although the Ti d_{xy}, d_{yz}, and d_{xz} orbitals point between the metal-ligand axes, the sum of their squares points towards the corners of the $SrTiO_3$ cube-unit cell and not towards its edges.

[74] A. Diefenbach, F. M. Bickelhaupt, and G. Frenking, J. Am. Chem. Soc. **122**, 6449 (2000).

[75] V. Turkowski, N. Ud Din, and T. S. Rahman, Computation **5**, 39 (2017).

[76] N. A. Pike, B. Van Troeye, A. Dewandre, G. Petretto, X. Gonze, G-M. Rignanese, and M. J. Verstraete, Phys. Rev. B **95**, 201106(R) (2017).

[77] D. K. G. de Boer, C. Haas, and G. A. Sawatzky, Phys. Rev. B **29**, 4401 (1984).

[78] C.-H. Chang, X. Fan, S.-H. Lin, and J.-L. Kuo, Phys. Rev. B **88**, 195420 (2013).